Experimentally Analyzing Diverse Antenna Placements and Orientations for UAV Communications

Mahmoud Badi, John Wensowitch, Dinesh Rajan, *Senior Member, IEEE*, and Joseph Camp, *Member, IEEE*

***Abstract*—A vast array of potential applications is emerging for drones and other devices to collaborate from disaster relief and search and rescue missions to smart agriculture and IoT systems. As drones move across multiple altitudes, they must have the ability to communicate across any direction in a three-dimensional (3D) space. However, due to the heterogeneous nature of the drone body and its interaction with the mounted antennas, different antenna positions on the drone can result in variations in the radiation pattern. While there have been a fair number of airborne communication works, few consider the role that antenna positioning has on the resulting transmission along the azimuth and elevation planes. In this work, we study the effects of the drone body and various antenna placements on the radiation pattern and fading of drone-based channels. Through systematic anechoic chamber and in-field measurements, we show that the drone body alters the radiation pattern of the mounted antennas, rendering the common assumption of a constant azimuth radiation pattern invalid. In addition, the body increases polarization mixing of drone-based channels, resulting in significant degradation of the cross-polarization discrimination (XPD). Hence, we propose using *effective* radiation pattern and XPD values instead of relying on measurements and/or assumptions that disregard drone-antenna interaction. We then analyze the shadowing and losses associated with the drone body for many antenna setups at various elevation angles and show that when mounted on the opposite side from the ground transmitter, shadowing increases with relatively-higher drone elevations. To account for these body-induced effects, we introduce *rotational loss* that results in better prediction results of the large-scale fading behavior compared to conventional models that neglect these body effects. Then, we analyze the small-scale fading for various antenna setups and show that the Rician K-factor is strongly dependent on elevation for polarization-matched vertical links, while it is approximately flat for cross-polarized links. To do so, we conduct a set of drone-to-drone (DtD) experiments at high altitudes with no surrounding reflectors and compare results to those obtained by our ground-to-drone (GtD) measurements. We find that, while at low elevations the ground can reduce the K-factor by 10 dB, at higher elevations, small-scale fading is dominated by the antennas, not the ground.**

***Index Terms*—MIMO, cross-polarization discrimination, drone-to-drone channels, UAV body effects, 3D communications.**

Manuscript received April 10, 2020; revised August 18, 2020 and October 8, 2020; accepted October 11, 2020. Date of publication October 19, 2020; date of current version January 22, 2021. This work was supported in part by NSF under Grant CNS-1823304 and in part by the Air Force Office of Scientific Research under Grant FA9550-19-1-0375. The review of this article was coordinated by Prof. S. Coleri. *(Corresponding author: Mahmoud Badi.)*

The authors are with the Department of Electrical and Computer Engineering, Southern Methodist University, Dallas, TX 75275-0221 USA (e-mail: mbadi@smu.edu; jwensowitch@smu.edu; rajand@smu.edu; camp@smu.edu).

Digital Object Identifier 10.1109/TVT.2020.3031872

I. Introduction

DUE to their low cost, ease of on-demand deployment, and ability to maintain position or move in any direction, drone investment has surged in recent years with a projected global market of $43 billion by 2024 [1]. Drones are becoming a viable option and are being used and tested in many applications such as entertainment [2], water sampling [3], interference management, public safety, smart agriculture, and disaster relief [4], [5]. Furthermore, as drones prepare to communicate in swarms, carry 5G traffic, and be integrated into IoT applications [6], drone-based multiple antenna systems that offer higher throughput and more robust airborne links are becoming more attractive than ever. Studies that focus on drone-based multi-input, multi-output (MIMO) channels are now surging and spanning a wide range of research areas, such as three-dimensional (3D) channel modeling [7], [8] and measurement-based evaluation [9]–[11]. Depending on the application, mounted antennas can be of differing types, have various orientations, and be placed at diverse drone-body locations, resulting in a variety of outcomes for the radiation pattern, the antenna's ability to distinguish between orthogonal components (measured by cross-polarization discrimination or XPD), and significantly impacting the capacity and diversity gains of cross-polarized MIMO systems.

Unfortunately, when it comes to research works that tackle drone-based channels, the radiation pattern of the used antennas have been mostly disregarded with the exception of a few works on large- and small-scale fading effects in drone-based wireless channels [12]–[18], [20], [25]. However, in all of these studies, the radiation pattern of the mounted antennas in the azimuth plane is assumed to be constant, or presented with no analysis of the possible effects on experimental outcomes [18], [19], [23]. In addition, the presence of buildings and reflecting objects in these studies makes it difficult to disentangle the role of the drone-mounted antennas from the impact of surrounding objects on fading severity. As a result, comprehensive measurement campaigns that lead to a broader understanding of drone-induced effects and more realistic channel models in Drone-to-Ground (DtG), Ground-to-Drone (GtD) and Drone-to-Drone (DtD) channels are still needed [22].

In this work, we study the role of the drone body and different antenna positions and orientations on (i) the radiation pattern, (ii) large-scale fading, and (iii) small-scale fading of drone-based wireless channels. Via systematic anechoic and

in-field experimentation, we quantify the significant degree to which the assumption of a constant azimuth radiation pattern for drone-mounted antennas inaccurate. We prove that the drone body can significantly change the radiation pattern of mounted antennas and also change co-polarized and cross-polarized channels, resulting in significant degradation of XPD. As a result, diversity gains and achievable MIMO capacity of cross-polarized drone-based systems are fundamentally altered.

To address how the orientation and location of drone-mounted antennas can affect the large- and small-scale fading nature of drone-based channels, we minimize environmental effects by conducting a series of high-altitude, line-of-sight (LOS) experiments in an almost building-free environment in Taos, New Mexico. We show that the drone body can increase the standard deviation of the shadowing parameter for polarization-matched vertical links. We also show that when the antenna is mounted on the opposite side of the receiving drone from the transmitter, the extra losses induced by the drone body need to be included in conventional models for accurate predictions. We do that by analyzing and modeling the impact of the drone rotation on the average channel gain/loss and show improvements of up to 85% in prediction accuracy with rotational aspects taken into account.

Then, we move to characterizing the small-scale fading of these drone-based channels in terms of the Rician K-factor. We show that the K-factor is strongly dependent on elevation for polarization-matched vertical links, while it is approximately flat for cross-polarized links. To isolate the impact of position and orientation of the drone-mounted antennas and not confuse that with fading caused by the ground, we compare results of the GtD experiments to those obtained by another set of DtD experiments and find that ground reflections can reduce the K-factor by approximately 10 dB. However, as we move to higher altitudes, the K-factor observed by both experiments becomes approximately the same, indicating less of a role for the ground compared to the actual antenna location and orientation. To the best of our knowledge, this is the first study to provide a systematic and comprehensive understanding of these fundamental drone-related issues.

The contributions of this paper are summarized as follows:

- We quantify, via anechoic chamber measurements, the effect of the drone body on the azimuth radiation pattern of omnidirectional antennas and find that, while the measured azimuth pattern is approximately constant for antennas in isolated mode (not mounted on a drone), it can be reduced by up to 10.25 dB when the same antennas are mounted on a drone. This finding proves that the assumption of a constant azimuth radiation pattern when dealing with drone-mounted antennas is no longer valid.
- We measure the co-polarized and cross-polarized radiation pattern of various antenna placements on the drone and show that the drone body can significantly impact channel depolarization and reduce XPD by an average of 15 dB compared to the XPD of an isolated antenna in the absence of a drone body.
- We show that there is an additional loss term caused by the drone body that needs to be accounted for unless the antennas on the transmitter and receiver are mounted on sides that face each other. This body-induced loss is found to be elevation-dependent for polarization-matched vertical links. We propose a model that describes this rotational loss and show that our model can be 85% more accurate than conventional models that neglect this body-induced effect.
- To understand how the orientation and location of drone-mounted antennas can affect small-scale fading, we characterize the Rician K-factor of the GtD channel and find that polarization-matched vertical links exhibit strong dependency on elevation, while cross-polarized channels result in an approximately flat behavior when elevation changes are considered. Then, by comparing a set of DtD experiments to our GtD experiments, we find that ground reflections can cause a degradation in the K-factor by up to 10 dB.
- Even though all of our experiments are conducted in LOS, we show that an antenna spacing of 0.67λ results in a correlation coefficient of less than 0.7 regardless of antenna orientation. In terms of diversity, this indicates achievable diversity gains in the range of 9.5 to 11.5 dB with basic selection or maximal ratio combining techniques.

The paper is organized as follows. Related works are discussed in Section II. In Section III, we discuss the system and channel model. In Section IV, we present our anechoic chamber and in-field results, discussing the effects of the drone body on the radiation pattern and XPD of the mounted antennas. We then explore shadowing and angle-dependent losses due to the drone body and mounted antenna locations in Section V. Then, in Section VI, we characterize the role of the drone-mounted antennas on small-scale fluctuations in GtD and DtD channels. Concluding remarks are presented in Section VII.

II. Related Work

Broadly speaking, literature related to drone communications can be classified into two main areas: (i) models that cover optimal placement, efficient deployment, and simulations that test different scenarios of trajectory and user mobility [45]–[50], and (ii) measurement-based studies that investigate the wireless channel in the uplink or downlink direction between a flying drone and a fixed or a moving node on the ground or in the air. The wireless channel in these measurement studies can be categorized as an air-to-ground (AtG), ground-to-air (GtA) or air-to-air (AtA) channel, depending on the nature of the target node.[1]

AtG channels. Many works have investigated the wireless channel between a hovering drone and a ground user with emphasis on how distance and antenna orientation can affect the received power or throughput at the ground node [13]–[15], [30]. The AtG channel at ultra-low drone altitudes was characterized with different settings of user equipment (UE) locations [23]. The AtG channel was studied after building a MIMO system that supports instantaneous measurements at different receiver locations on the ground as well as beamforming from the drone

[1]While we would consider GtD/DtD a subset of GtA/AtA, we specifically use the former in this work to emphasize on the impact of the drone body on the wireless channel.

transmitting antennas [10], [11], [41]. Shadowing was measured at diverse frequencies, and a modification to the conventional path loss model was made to account for the obtained frequency-dependent variations [44]. In [43], shadowing caused by the body of a medium size fixed-wing aircraft was found to reach values of up to 30 dB.

GtA channels. Due to its unique body structure, continuous movement, and limited space on board, in addition to being envisioned in scenarios where multiple antennas on the drone are receiving packets from ground sensors or users, the receiving channel characteristics of multiple drone-mounted antennas have been of interest. For example, the channel between a ground transmitter and an aircraft flying at speeds around 120 km/hour was studied, and it was concluded that placing two antennas one above and another below the aircraft body can result in throughput improvements [39]. Correlation coefficients and diversity gains were studied for various antenna positions on a fixed wing structure and packet delivery improvements of up to 32% were achieved [16]. An array of multiple antennas at the ground was used to sound the channel in a forest environment, where a fixed wing UAV flew at different altitudes and with co-polarized and cross-polarized links, and measurements of the cross-polarization discrimination were made at those altitudes with some emphasis on the achieved gains using different antenna orientations [40]. In the same context of GtA channels, the work by Akram et. al. has resulted in an angle-dependent model for cellular-to-UAV channels, where the received power and the shadowing parameter can change based on the depression angle [32].

AtA channels. The channel in a drone-to-drone LOS scenario was studied at different altitudes, and an extension of the Rician model was developed, where the variance of the received power, which describes multipath components, was modeled as a function of the drone altitude [18]. We investigated the impact of relative direction on received signal while two drones fly at the same altitude [21]. The throughput of a two-hop network was studied under different scenarios of mobility [31]. While all of the above mentioned studies target important issues that can help in understanding drone communications, none of them consider how signal reception on a drone with multiple antennas can be affected by the drone body and its rotation. In addition, the environments in which the above mentioned experiments took place and the scenarios involved make it difficult to isolate the impact of the antennas and the drone body on the presented results. In contrast, this work focuses on the impact of the drone body and drone-mounted antennas via carefully-designed experiments.

III. System and Channel Model

In this section, we describe the system and channel model in the view of our comprehensive analysis framework. This framework targets the fundamental issues related to wireless channels, starting with the radiation pattern and XPD measured via anechoic chamber and in-field experiments in a 2D space. Then, large-scale fading is studied in terms of shadowing and angle-dependent losses for the drone-mounted antennas at many elevation angles with different heading directions (i.e., in 3D space). Finally, to understand the small-scale fading nature of the drone-based links, we characterize the the Rician K-factor for many GtD and DtD topologies. Through this systematic approach, we have a comprehensive view of the channel of drone-based antenna systems. This section describes the concepts needed to understand our work.

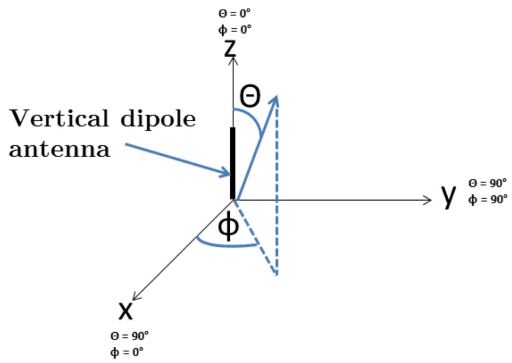

Fig. 1. Vertically oriented dipole antenna.

A. Antenna Radiation Pattern Modeling

The antennas used in our characterization framework are linearly-polarized omnidirectional dipole antennas (VERT2450). To explain how we model the radiation pattern of this antenna, we show a vertically-oriented dipole antenna along the z direction in Fig. 1. The radiation pattern in the elevation plane is measured from the vertical (z) direction and described in the spherical coordinate system in terms of Θ. Conversely, the horizontal (azimuth) plane is described in terms of Φ. In the case of a vertically-mounted dipole, the radiation pattern[2] is given by [56], [57]: $G_z = \sin\Theta$, with no azimuth variation. Note that this assumption of no azimuth variation for omnidirectional antennas will be proven here to no longer hold true when the antenna is mounted on a drone. If mounted horizontally (i.e., over the x-y plane), the pattern becomes: $G_y = -\cos\Theta \sin\Phi$. We use the notation of G_{VV} to indicate the gain product of vertical Tx-Rx antennas (VV link), whereas G_{VH} is used to indicate the gain product of a vertical Tx and a horizontal Rx antenna (VH link). Note that we are interested in the elevation angle θ from the xy plane, which is computed as $\theta = \frac{\pi}{2} - \Theta$. In our experiments, this elevation angle, θ, can be calculated using $\theta = \arctan(l/d_h)$, where l is the altitude of the Rx drone, and d_h is the horizontal separation distance. Given these models, the gain product for a VV link becomes $|G_{VV}| = \cos^2(\theta)$. For a VH link, the gain product becomes $|G_{VH}| = \cos(\theta)\sin(\theta)\sin\phi$. With the horizontal dipole mounted in the y direction, $\sin\phi = \sin\frac{\pi}{2} = 1$, and we are left with $|G_{VH}| = \cos(\theta)\sin(\theta)$. If we use these models and compare them to the manufacturer's datasheet [58], we find that the average difference between the two methods across the considered elevation angles is 1.14 dB with a standard deviation

[2]Radiation pattern and gain are used interchangeably in this work.

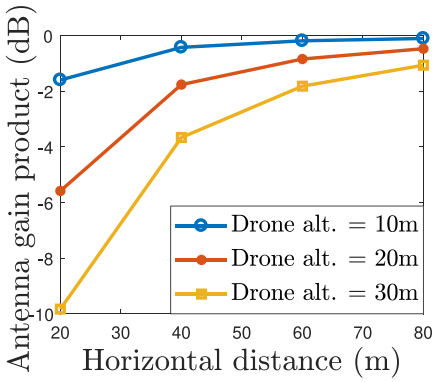

Fig. 2. Tx-Rx antenna gain product for omnidirectional dipole antennas at different elevation scenarios. At some angles, losses caused by radiation pattern misalignment can be greater than distance-based losses.

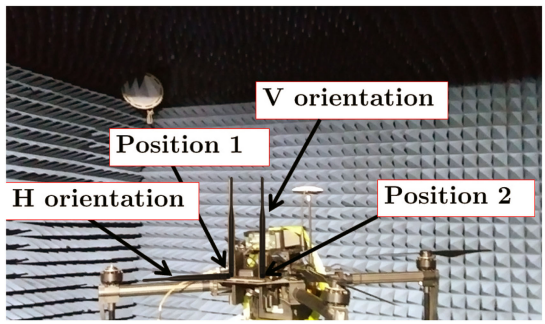

Fig. 3. Anechoic chamber setup. The two antenna positions/locations are shown on the drone body.

of 2.25 dB. Using this model allows us to study elevation dependencies with relatively low errors.

B. Cross-Polarization Discrimination (XPD)

Due to the limited space on a drone, as in many other compact devices, a scenario with dual-polarized antennas or cross-polarized antenna setups is quite realistic. With cross-polarized configurations, XPD becomes an important parameter to consider since it can affect how we analyze and model polarized MIMO channels [24], [26]–[28], [34]. Depending on the signal-to-noise ratio (SNR) and the desired application, the impact of XPD on the cross-polarized MIMO channel can be perceived differently. For example, if increasing the channel capacity is desired, then high XPD values at high SNR levels can theoretically double the spectral efficiency. If, on the other hand, XPD is poor (e.g., 0 dB), spatial multiplexing using the two orthogonal components is not possible. However, this poor discrimination could mean a rich scattering environment where diversity gains could be extracted. For the above reasons, it is interesting to investigate the impact of the drone body and the different antenna placements on polarization mixing and consequently, XPD. To the best of our knowledge, aside from our previous study [21], XPD on drones has not been explored.

To characterize XPD on drones, we conduct anechoic chamber experiments and measure the received power for co-polarized and cross-polarized channels and calculate the difference in received power as XPD. This experiment is done for two antenna setups: (i) isolated and (ii) drone-mounted. In the isolated scenario, only the antenna exists at the receiver side of the chamber. In the drone-mounted scenario, the antenna is mounted on the drone at either position 1 or position 2 (see Fig. 3). In all scenarios, XPD is calculated as the ratio of the amount of power received in the co-polarized versus cross-polarized directions [28]:

$$XPD = P_{copol}/P_{xpol} \tag{1}$$

The co-polarized radiation pattern is obtained by orienting the transmit and receive antennas horizontally and automatically rotating the receiving antenna in 1.8° increments. Through this procedure, we get P_{HH}, where the first and second subscripts indicate the orientation of the transmitter and receiver antennas, respectively. To acquire the received power in the cross-polar plane, the transmitting antenna is vertically-oriented and the receiving antenna is kept horizontal. The same procedure is then repeated, and P_{VH} is obtained per iteration. Calculating the ratio of $\frac{P_{HH}}{P_{VH}}$ gives us XPD. In this work, we show that mounting antennas on drones not only alters the radiation pattern in the azimuth plane significantly, but also results in a significant degradation in XPD. Furthermore, we show that the in-field XPD in a DtD LOS channel can vary from one relative direction to another.

C. Received Signal Strength (RSS) and Angle-dependent Loss

Since our main focus is on understanding how the drone body affects the channel for various antenna placements, all experiments are conducted with a clear LOS between the transmitter and receiver. We transmit a continuous wave (CW) signal at a carrier frequency of 2.5 GHz and power of 6.2 dBm. The transmitter and receiver are the battery-operated Universal Software Radio Peripheral (USRP) software defined radio devices called E312. The received signal at each RF chain at the receiver USRP is down-converted, baseband processed, and stored in the USRP's memory in the form of I/Q samples. From the recorded I/Q samples, we calculate the instantaneous received signal strength (RSS) in dBm for antenna/Rx l as $RSS = P_r(\text{dBm}) = 10\log\frac{P_{rms}}{1(mw)}$, where $P_{rms} = (r_l/\sqrt{2})^2/50\Omega$. The received signal envelope (r_l) is calculated as $|r_l(t)| = \sqrt{r_I(t)^2 + r_Q(t)^2}$. This RSS is a function of the transmitted power P_t, Tx/Rx antenna radiation patterns (G_T and G_R), carrier wavelength λ, distance d, and polarization loss factor ψ and is given by the Friis formula [56]: $P_r(\theta,\phi) = P_t G_T(\theta,\phi) G_R(\theta,\phi)(\frac{\lambda}{4\pi d})^2\psi$. In co-polarized links, the polarization of the incident electric field matches the polarization of the receiving antenna, and no losses are incurred. On the other hand, in a cross-polarized link, due to the mismatch between the direction of the incoming electric field and the receiving antenna orientation, the received signal is reduced. However, due to antenna imperfection and environmental factors (reflection and scattering), energy can still be collected by cross-polarized links. In fact, we show that due to the drone body effect on mounted antennas, there is little

distinction between co-polarized and cross-polarized channels. For a polarization-matched link, the free-space received power is given by:

$$P_r(\text{dBm}) = P_t(\text{dBm}) + 10\log(G_{T,R}) + 20\log\left(\frac{\lambda}{4\pi d}\right) \tag{2}$$

Here, $G_{T,R} = G_T G_R$ is the transmit-receive antenna radiation pattern product discussed above. To account for fluctuations caused by the drone body, equation (2) should include a shadowing term ξ_s, which is usually modeled as a normally-distributed random variable with zero mean and a standard deviation of σ_s (i.e., $\mathcal{N}(0, \sigma_s)$). We will show later how this shadowing term can change with the drone-heading direction for some antenna orientations/locations. Finally, as the drone can rotate in any direction while hovering at a fixed altitude, we find that the average RSS can be reduced due to drone body blockage. As a result of this body blockage, the received power will be reduced by a term denoted here as $\Gamma_\phi(\theta)$. The dependency of $\Gamma_\phi(\theta)$ on elevation angle will be discussed in Section V-C. When the shadowing and body-induced losses are added to equation (2), it becomes:

$$P_r^{VV} = P_t + 10\log(\cos^2\theta) + 20\log\left(\frac{\lambda}{4\pi d}\right) + \xi_s - \Gamma_\phi(\theta) \tag{3}$$

For the VH link, the received power becomes:

$$P_r^{VH} = P_t + 10\log(\cos\theta\sin\theta) + 20\log\left(\frac{\lambda}{4\pi d}\right) + \xi_s - \Gamma_\phi(\theta) \tag{4}$$

Angle-dependent vs. Distance-dependent Loss: It is important to understand that in some scenarios, angle-dependent models are more convenient and help to accurately characterize the behavior of drone-based links over conventional, distance-based models. This observation was mentioned in other works, but no examples were given to quantify the effect [32]. Here, we provide an example scenario where angle-based models greatly outperform distance-based models. In this example, a ground node communicates with a hovering drone with a fixed horizontal distance of $d_h = 20$ m. The drone moves from an altitude of $l = 10$ m to $l = 30$ m in 10-m increments. The elevation angles created are, respectively, 26.5°, 45°, and 56.3°. If we exclude the radiation pattern effects, the reduction in power due to the increase in the separation distance from $d = \sqrt{(}20^2 + 10^2) = 22.3$ m to $d = \sqrt{(}20^2 + 30^2) = 36$ m is approximately 4 dB. If we model the elevation pattern of each of the Tx/Rx antennas as $|\cos(\theta)^2|$, the loss just due to the antenna pattern misalignment would be $10\log(\cos(\theta)^4) = 10\log(\cos(\tan^{-1}(\frac{l}{d_h}))^4) = 10$ dB. Hence, by excluding the radiation pattern in this scenario, the received power would be overestimated by 6 dB.

In an ideal scenario, the transmitter and receiver antenna are perfectly aligned (i.e., $\theta = 0°$), and the loss is 0 dB. The antenna gain product for the three altitudes and horizontal distances of up to 80 m is shown in Fig. 2. We can see that the effect of the gain product is greatest at small horizontal distances with high drone elevations (i.e., large elevation angles). As the horizontal distance increases for a fixed altitude, the elevation angle becomes smaller, resulting in a small antenna gain misalignment loss compared to losses due to the increasing distance. Since our 3D experiments characterize a fixed horizontal distance with varying altitudes, we henceforth consider an angle-dependent version of (3) and (4). Given that $d_h = d\cos\theta$, $|G_{VV}| = \cos^2(\theta)$, $|G_{VH}| = \cos(\theta)\sin(\theta)\sin\phi$, which at $\phi = \frac{\pi}{2}$ becomes $|G_{VH}| = \cos(\theta)\sin(\theta)$, and by subtracting P_r from P_t, the angle-dependent loss for the VV and VH links, after some manipulation, respectively, becomes:

$$L_{VV}(\theta) = 20\log\left(\frac{4\pi d_h}{\lambda\cos(\theta)^2}\right) - \xi_s + \Gamma_\phi(\theta) \tag{5}$$

$$L_{VH}(\theta) = 20\log\left(\frac{4\pi d_h}{\lambda}\right) + 10\log\left(\frac{1}{\cos(\theta)^3\sin(\theta)}\right) - \xi_s + \Gamma_\phi(\theta) \tag{6}$$

D. Small-Scale Fading Characterization

Since a LOS path exists in all of our experiments, the channel is assumed to be Rician and characterized accordingly. Therefore, we follow convention [51],[52] and model the channel as the sum of a steady, time-independent component of $\alpha + j\beta$ and a random-fluctuating component of $x(t) + jy(t)$, where $x(t)$ and $y(t)$ are zero-mean, Gaussian random variables with variance σ^2. If no LOS path existed, then, the specular component $\alpha + j\beta = 0$, and the received signal envelope would follow a Rayleigh distribution. However, since all of our experiments include LOS paths, the mean values of r_I and r_Q are not zero, but, instead, α and β, respectively, resulting in a Rician distribution for the received signal envelope. The Rician K-factor can be calculated from the samples of the received signal, as the ratio of the power in the main LOS component to that in the scattering, time-varying components. The Rician K-factor (in dB) can be calculated as:

$$K(dB) = 10\log_{10}\left(\frac{\alpha^2 + \beta^2}{2\sigma^2}\right) \tag{7}$$

Here, $\alpha^2 + \beta^2$ and $2\sigma^2$ are, respectively, the mean powers of the specular (LOS) and scatter components and can be found from the measured I/Q samples as follows. The mean values of the in-phase and quadrature components are respectively calculated as $\alpha = \mathbf{E}[r_I] = \frac{1}{N}\sum_{n=1}^{N} r_I(n)$ and $\beta = \mathbf{E}[r_Q] = \frac{1}{N}\sum_{n=1}^{N} r_Q(n)$, where n is the sample number. The variance of the in-phase or the quadrature component over a period of N samples is $\sigma_I^2 = \text{Var}[r_I] = \sigma_Q^2 = \sigma^2$. After finding these values, we calculate the K-factor according to equation (7). We choose to characterize the small-scale fading over a period of 3000 samples, which corresponds to approximately 93.7 ms.

IV. Impact of Drone Body and Various Antenna Placements on Radiation Pattern and XPD

To quantify the impact of the drone body and antenna placement on the radiation pattern and XPD, we conduct multiple controlled anechoic chamber and in-field experiments. We show that placing antennas on drones is a nontrivial task due to the interaction of the drone body with mounted antennas.

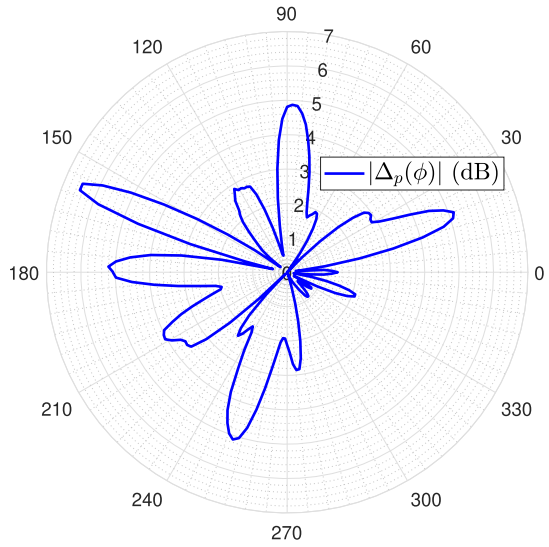

Fig. 4. Difference in received power by the two vertically mounted antennas on position 1 and 2 in the anechoic chamber.

A. Radiation Pattern of Drone-Mounted Antennas

Due to its unique structure and the various possible locations for antenna mounting, the drone body can affect the radiation pattern of the mounted antennas. This has been explored in our recent work [21] and one other study [23]. However, in the latter study, the experiment was not performed in an anechoic chamber, and the results are subject to environmental changes. In addition, there was no emphasis on the antenna placement on the drone, and the results of the radiation pattern were not analyzed. In our previous work [21], we only tested and presented limited results for one antenna position on the drone. Here, we test multiple antenna locations and show that different antenna placements on the same drone can result in considerable changes in the radiation pattern at some angles.

The drone with the two antenna locations in the chamber is shown in Fig. 3. Note that to mimic the structure of the drone in our in-field experiments, the same experiment's hardware is mounted on the drone and explained in Section V-A. In the isolated case, only the antenna is mounted at the receiving end of the chamber, and its radiation pattern is measured. Then, in the antenna-on-drone scenario, we place the antenna on the drone according to the positions shown in Fig. 3 and study the resulting radiation pattern. The transmitting antenna is fixed and vertically-oriented while the vertically-receiving antenna automatically rotates over the azimuth plane (ϕ) in 1.8° increments as the received power is being recorded.

The results of the anechoic chamber experiment are shown in Fig. 5(a). In this figure, "simulated" indicates a constant-azimuth radiation pattern, which is the general assumption made in most drone-related literature. The antenna-only measurements represent the measured values using the antenna in isolated mode, meaning only the antenna exists in the chamber. We see, as expected, strong symmetry and the radiation pattern follows closely the constant-azimuth pattern assumption made in literature. If we mount the antenna on the drone, however, the results become significantly different, and the constant-azimuth pattern is no longer valid. This variation can be clearly seen in the blue and red lines that indicate the measured power values of the drone-mounted antennas, where differences from the isolated (antenna-only) scenario can reach up to 10.2 dB. In addition, there is also a difference in radiation pattern due to different antenna positions on the drone (see Fig. 3 for antenna positions). This difference can be seen by inspecting the red and blue lines in Fig. 5(a), which correspond to antenna position 1 and 2, respectively. In this figure, we point to an angle where we can see a difference of 6.5 dB, which is the maximum difference in radiation pattern due to different antenna locations on this drone. One might ask the question why such differences exist even though the antenna positions look symmetrical on the drone body. The answer is as follows: when the drone body starts to rotate, each Rx antenna sees a slightly a different signal level because each position exhibits a different part of the drone body (i.e., obstacle). This difference is clear if we look at the difference in received power by the two antennas – for the whole 360 degrees azimuth plane (shown in Fig. 4). As we can see in the figure, at 0 degrees (Facing tx antenna) there is approximately no difference. As the drone rotates, however, differences in rx power manifest and cause the values of received power to slightly differ. In this figure (Fig. 4), $|\Delta_p(\phi)|$ is the absolute difference in received power between the two mounted antennas at positions 1 and 2, respectively.

TABLE I
IMPACT OF DRONE BODY ON CO-POLAR RADIATION PATTERN VALUES

Experiment	Average Loss	Maximum Loss
Antenna on Drone (position 1)	2.57 dB	8.34 dB
Antenna on Drone (position 2)	3.27 dB	10.25dB

The average and maximum reductions in radiation pattern for the two antenna positions are summarized in Table I. These average and maximum losses are taken over the whole azimuth (ϕ) plane. The loss is simply the difference between the azimuth power in the isolated (antenna-only) scenario and the drone-mounted antenna scenario. We see that these losses can reach up to 10 dB, with an average of up to 3.3 dB. It is important to note that while this reduction might not seem significant, on average, reductions of more than 5 dB appear multiple times over the whole azimuth plane for a fixed antenna position. We conclude from these controlled experiments that antenna placement decisions on drones, trivial as they might seem, can considerably impact wireless channels in drone-based networks, where rotating a drone or switching to a nearby antenna on the same drone, can lead to significantly stronger channels.

B. Anechoic Chamber XPD

After realizing the impact of the drone body on the azimuth radiation pattern, a natural question comes to mind: Is the local scattering caused by the drone body strong enough to cause polarization mixing? If so, by how much? Here, we answer these questions.

The results of the measured co-polarized and cross-polarized channels for the antenna-only and antenna-on-drone (position

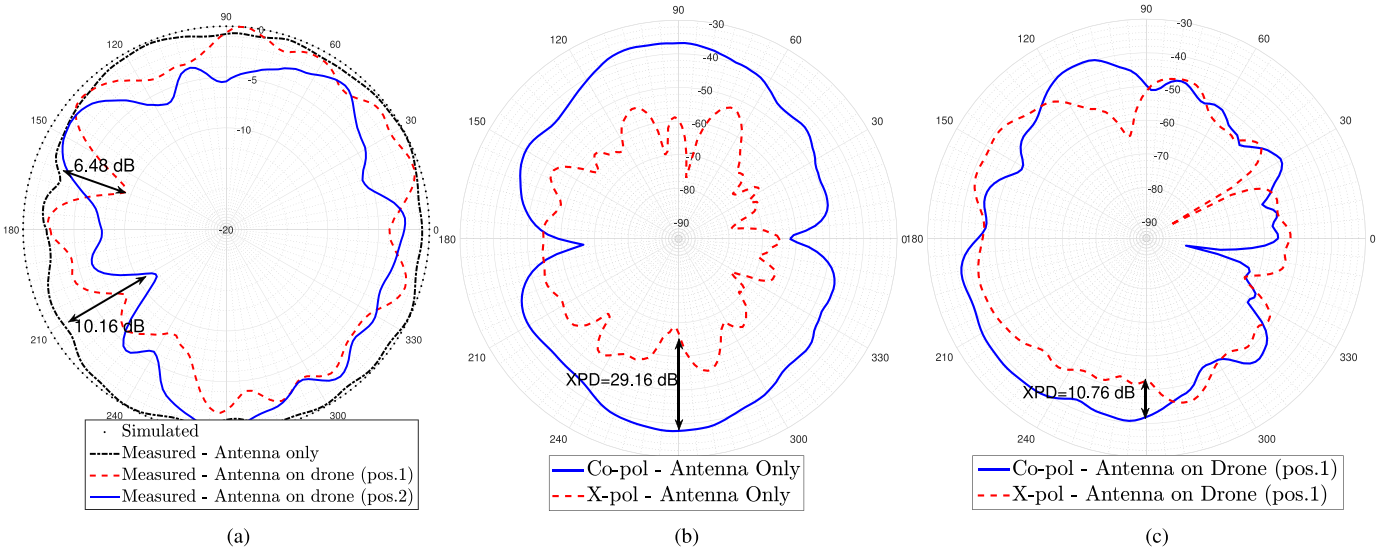

(a) (b) (c)

Fig. 5. (a) Azimuth radiation pattern for the simulated, antenna only (measured), and antenna on drone for two positions (measured). (b) The HH/VH co-polarized/cross-polarized radiation pattern for the antenna only setup: clear distinction between the two orthogonal polarizations exists. (c) The HH/VH co-polarized/cross-polarized radiation pattern for the antenna on drone setup (position 1): high polarization mixing exists due to the drone body.

1) scenarios are shown in Fig. 5(b)-5(c). Through a quick visual inspection, we can see that there is a clear distinction between the co-polarized and cross-polarized received powers in the isolated (antenna-only) scenario. This distinction, however, becomes almost nonexistent for the antenna-on-drone scenario. The disappearance of this distinction is due to higher polarization mixing between the vertical and horizontal components, caused solely by the drone body. This polarization mixing, according to the geometrical theory of channel depolarization [33], can be attributed to the local scattering and reflection caused by the drone body.

While there is an abundance of works on XPD and how it is affected by scattering objects [24], [34]–[38], none have investigated the drone body as the only source of polarization mixing. Here, we show that the drone body *by itself* can act as a source of scattering and reflection, demonstrated by significant reductions in XPD. For example, if we look at XPD at $\phi = 270°$, we can see that in the isolated scenario, XPD is 29.16 dB. In the drone-mounted scenario at the same angle, it is 10.76 dB for antenna position 1 and 11.25 dB at antenna position 2 (not shown here). Over all rotational angles, the average XPD for the isolated (antenna-only) scenario is $\overline{XPD}_{isolated} = 17.33$ dB. In contrast, the average XPD for antenna positions 1 and 2 is $\overline{XPD}_{pos.1} = 2.33$ dB $\overline{XPD}_{pos.2} = 4.71$ dB, respectively.

We believe that these are significant findings due to the impact that XPD can have on achieved capacity and diversity gains in MIMO applications that leverage cross-polarized channels [36], [37]. For example, an average XPD value of 0 dB means that the spatial multiplexing gain is limited. On the other hand, the same 0 dB value can indicate a richness of scatterers in the multipath environment, which leads to a low correlation coefficient and high diversity gains [34]. While it can be argued that these results are specific to this drone (DJI Matrice 100), the insight we gain from this study can be valuable for drone swarm designers or researchers who aim to model drone-based polarized MIMO channels. In addition, simulation tools, such as [29] can incorporate these findings through an *effective* antenna pattern and XPD lookup tables rather than treating the antennas as point objects, which is proven here to be highly inaccurate.

C. In-Field XPD

We now evaluate the impact of different drone relative directions on the measured XPD from a set of experiments conducted in our previous work [21], where more detailed description of the experiment is presented (omitted here due to limited space). The experiment is conducted with two drones at an altitude of 60 m above the ground. While the Rx drone is continuously hovering at a fixed location, the Tx drone moves in 20 m increments from one location to another until it reaches 100 m of separation distance. This Tx drone movement takes place in each of the four cardinal directions (North, South, East, and West). The Tx drone has one vertically-oriented (V) antenna, while the Rx drone is equipped with one vertical and one horizontal antenna that are connected to the same USRP and fed from the same local oscillator. Both drones face North throughout all experiments. The Rx vertical (V) antenna is mounted in position 1 in Fig. 3, while the horizontal antenna (H) is mounted in position 2, creating two links denoted as VV and VH from the transmitter to receiver. We can view the receiver as a dual-polarized system and use our measurements for the VV and VH channels to predict the in-field XPD at the receiver. We follow [24], [35] and calculate XPD as the difference in co-polarized and cross-polarized pathloss (i.e., $XPD = PL_{VV} - PL_{VH}$) and investigate how diverse Tx directions from the Rx can affect polarization mixing at the receiver. XPD is calculated for each hovering location, and the results are summarized in Table II. Note that in [21] we investigated the impact of relative Tx drone direction on RSS

TABLE II
XPD FOR DIFFERENT RELATIVE DIRECTIONS IN DTD CHANNELS

Direction	20m	40m	60m	80m	100m	Avg.
XPD_{North}	1.29	1.55	2.64	2.1	3.53	2.22
XPD_{South}	5.67	3.45	7.61	6.01	5.2	5.58
XPD_{East}	4.56	10.1	11.61	8.0	8.32	8.51
XPD_{West}	4.2	9.83	11.24	10.6	8.43	8.86

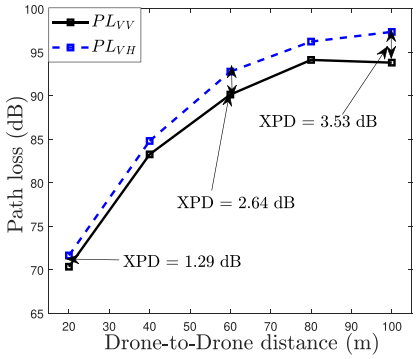

Fig. 6. Measured XPD values for the North scenario.

and found that RSS levels at the Rx drone can vary by as much as 15 dB as the Tx drone changes its relative direction from in front of to behind the Rx drone.

We see that XPD can considerably change if the transmit drone takes different relative directions from the receiving drone. For example, we see that the strongest measured XPD values are when the transmit drone is on the side (East or West), while the lowest value is when the transmit drone is North of the receiving drone (shown in Fig. 6). On average, the North XPD value is 6 dB less than that in the East or West and 3.3 dB less than in the South experiment. This result suggests that if the Tx drone is facing-away from the receiving drone, the transmitted polarization becomes almost independent from the received polarization. It is important to note that, while they fall approximately in the same range, the measured XPD values here are slightly different from the anechoic chamber results since the transmitter is actually mounted on a drone as opposed to just the antenna in the chamber. In addition, XPD here is measured using two antennas mounted on the Rx drone. In the chamber, we changed the orientation of the Tx antenna to get the cross-polar radiation pattern with the Rx antenna fixed. However, the focus here is not on replicating the chamber measurements in the field but to demonstrate the influence of different relative drone directions on XPD, which is found to vary by up to 10 dB (from 1.29 to 11.61 dB). This 10 dB reduction in XPD could be detrimental to spatial multiplexing gains and the capacity of dual-polarized MIMO systems on drones. It might be worth mentioning that, in addition to these experiments where the two drones are at a fixed altitude, we have performed another set of experiments that investigate the impact of relative altitude and elevation angle on received signal levels and XPD for various antenna orientation setups at the receiver. We found that for vertical Tx and Rx antenna, the RSS can vary by up to 30 dB as the Rx drone moves from one location of the same altitude as the Tx drone to directly below or above it. Horizontal antennas, however, record 12 to 20 dB higher RSS levels when the Rx drone is below or above the Tx drone. With regards to XPD, similar values were found to the ones obtained in this work. We refer the interested reader to [21] for more details.

V. IMPACT OF DRONE ROTATION WITH VARIOUS ANTENNA PLACEMENTS IN 3D SPACE

Previously, we characterized the effects of the drone body and various antenna placements on the channel with the receiver drone being at the same altitude as the transmitter drone. In other words, we only studied the azimuth plane (elevation angle $\theta = 0°$). However, in some scenarios, such as a drone swarm or a UAV-assisted network, a drone can be in an arbitrary relative location in 3D space. For example, consider a scenario where a drone provides some service to two users on the ground. In this scenario, the antenna is mounted on the same side of the drone as one user (i.e., facing) but on the other side of the drone from a second user (i.e., facing-away). The shadowing and received signal levels seen by each user would likely be different. With this in mind, one might ask the following questions: How do these effects behave at other elevation angles? Are they the same for vertical and horizontal drone-mounted antennas? To answer these questions, we conduct multiple GtD LOS experiments varying the elevation and azimuth angles of the drone. We analyze shadowing and average rotational loss and provide a model that captures these body-induced effects. This part of the study could be valuable for algorithms that try to find the optimal heading direction for UAVs [45], [46] when communicating with ground nodes.

A. Experiment Procedure

The experiment procedure is illustrated in Fig. 7(a). The transmitter is located on the tripod at a height of 1 m above ground level. The receiving drone is positioned at a fixed horizontal distance of $d_h = 20$ m. The drone navigates to each point of interest and hovers there while directly facing towards (and away from) the transmitter. The drone maintains a stable hovering position at each location for 20 seconds per heading direction. As the drone ascends in altitude, different elevation angles are realized by $\theta = arctan(l/d_h)$, where l is the altitude of the drone with respect to the transmitter.

At each hovering location, I/Q samples are collected for both RF chains for the facing and facing-away directions. By leveraging the log files generated by the shell and python scripts that we implemented on the USRPs, we are able to accurately match the timestamps of the received data to the location and direction of the drone. Sensor measurements are used in the offline processing of the received samples, where we splice the dataset according to time, altitude, heading direction, and GPS location. Three (3) experiments are carried out: V-VV, V-VH, and V-HD. The first letter is the transmitter's antenna orientation, and the second two letters are, respectively, the orientations of the first (antenna position 1) and second (antenna position 2) receiving antennas. V, H, and D are, respectively, vertical up, horizontal, and vertical down. Fig. 7(b) depicts the antenna setup at the receiver for the V and D orientations. The H orientation is

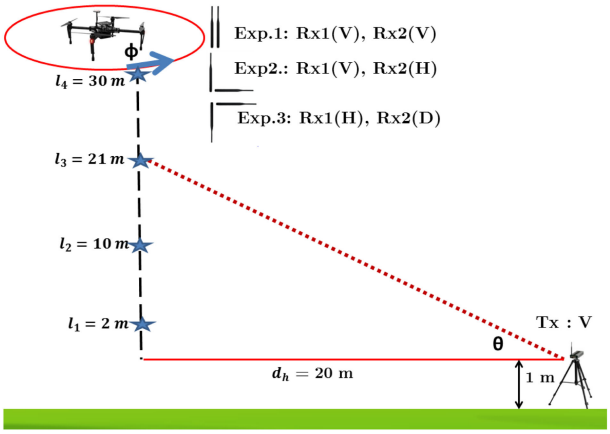

(a)

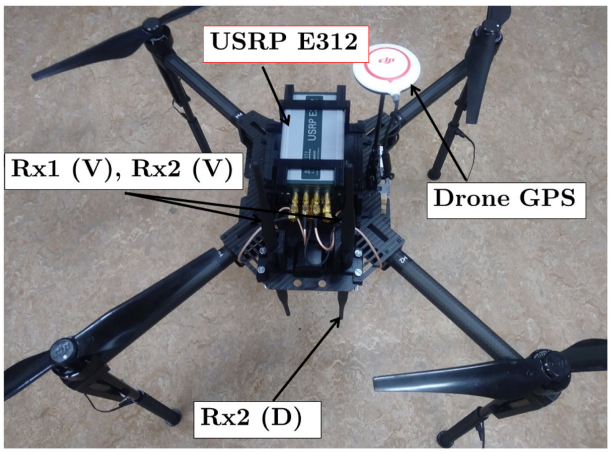

(b)

Fig. 7. (a) GtD Experiment setup and hovering locations for the Rx drone. (b) Rx drone structure and the mounted V and D antennas.

shown in Fig. 3. In the V-VH experiment, H is in position 2. In the V-HD experiment, H is in position 1. We refer to a Tx-Rx link in an experiment as VX where V is the transmitter orientation (which is always V), and X is the receiver orientation. For example, VH indicates a vertical Tx and horizontal Rx on the drone.

B. Drone Description

The body and frame of the Matrice 100 is made up of various lightweight materials including carbon fiber, aluminum, plastic, and steel. The frame is braced with aluminum brackets and held together with steel screws. The majority of the frame, including the top and bottom plate as well as the propeller arms, is constructed out of epoxy hardened carbon fiber weave. Carbon fiber is known to shield radio frequencies but the degree of shielding largely depends on various characteristics of how the carbon fiber is manufactured [59]. The exact characteristics of the carbon fiber used by DJI are unknown to us and this limits our ability to fully model its effects. While not the focus of this investigation, our anechoic chamber experiments should capture the behavior that this particular drone body presents.

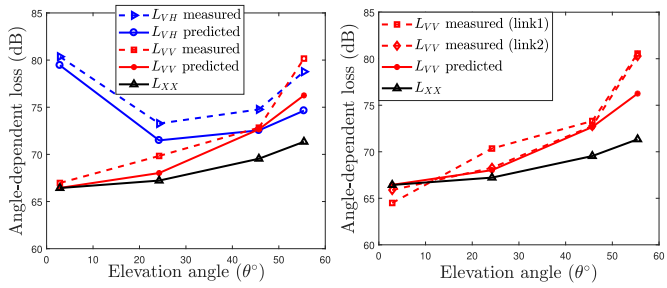

(a) (b)

Fig. 8. Measured and predicted values of the angle-dependent loss for the (a) V-VH and (b) V-VV experiments.

C. Elevation Dependency

Before we characterize the impact of drone rotation at different elevation angles (i.e., θ), we first investigate the impact of elevation on the received signal for vertical and horizontal antenna orientations. Using the developed angle-dependent models, with $|G_{VV}| = \cos^2(\theta)$ and $|G_{VH}| = \cos(\theta)\sin(\theta)$, we analyze the measured and predicted values of this loss as the drone hovers at different elevation angles from the ground.

The angle-dependent loss for V-VH and V-VV experiments is shown in Fig 8. We notice that experiment results closely follow our analytical models. For the vertically-oriented antenna (VV links), loss is minimum at 3° elevation. The loss increases as the drone flies to higher altitudes. The increase in loss is due to gain misalignment of the mounted antennas in addition to the distance impact. This behavior is consistent and can be seen in all vertically-oriented receivers: see Fig. 8(a) and the VV loss in Fig. 8(b).

However, the results are different for the horizontally-receiving antenna (VH links). We see that the highest loss is recorded at 3° elevation. Then, as the drone moves to higher altitudes (30° to 45° range), this angle-dependent loss gets smaller. Then, the loss goes up again at $\theta = 55°$. This behavior can be better understood based on the analytical models that we developed. The measured values shown in these graphs are the difference between the transmitted power and the average received power when facing the transmitter.

The facing-away scenario will be dealt with separately. The predicted values are given by L_{VV} (equation (3)) for the VV link and L_{VH} (equation (4)) for the VH link. Here, the standard deviation of the shadowing parameter is chosen to be $\sigma_s = 2$ dB. Although the exact shadowing value might vary in different situations, based on numerous experimentation over multiple years, we found that a 2 dB value to be appropriate. The body-induced loss ($\Gamma_\phi(\theta)$) is assumed to be 0 dB. This body-induced loss will be a contributing factor when the drone is facing-away from the transmitter. The assumption here is that since the antennas are mounted near the edge of the drone, the elevation radiation pattern when facing a node is unaltered and can be modeled as above. We see that the angle-dependent models, because of their inclusion of the proposed radiation pattern models, capture the measured values of the angle-dependent losses to a good extent.

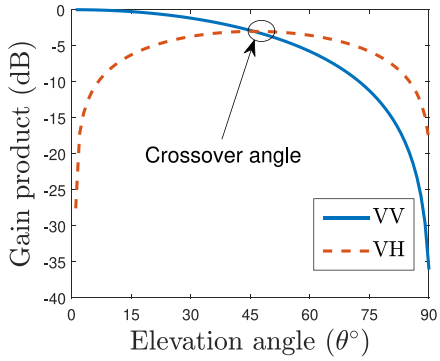

Fig. 9. Antenna gain product for VV and VH links and the crossover angle.

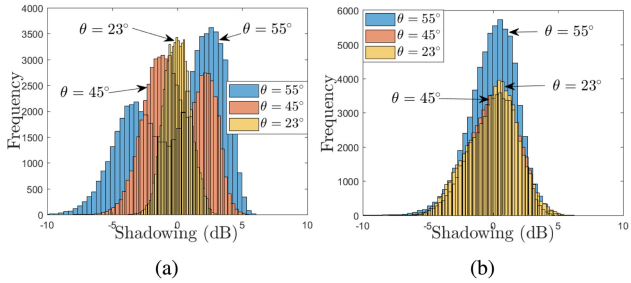

Fig. 10. Measured shadowing for (a) VV and (b) VH links when facing-away ($\phi = 180^\circ$). Higher elevations lead to higher body-induced shadowing in VV links.

In contrast, predictions provided by L_{XX}, which is simply the free-space path loss in addition to shadowing, is shown to be the least accurate due to its exclusion of the important radiation pattern effects.

Another observation is that around 45° elevation, we can see that VV and VH links exhibit similar losses, although cross-polarized. This effect can be explained if we equate G_{VV} to G_{VH} and solve for θ, which would give us an angle of $\theta = 45^\circ$. We refer to this as the cross-over angle, the angle at which a flip occurs in antenna gain product for VV and VH links. Fig. 9 illustrates the antenna gain product for the two links. We see that before this angle, VV links experience higher antenna gain product. However, after this angle, VH links have the higher antenna gain product, consequently resulting in lower angle-dependent loss values. This dependency on antenna gain product explains the behavior of the measured values and shows how understanding the radiation pattern of the used antennas is of paramount importance in drone-based links since significant differences can occur with minimal distance variations. In fact, when we measure the received signal at an elevation angle of $\theta = 90^\circ$ (i.e., the Rx drone directly above the transmitter, with a vertical separation distance of 20 m), we record a stronger signal of up to 20 dB greater for VH links compared to VV links [21].

D. Drone-Body-Induced Shadowing in 3D Space

Before quantifying the losses induced by the drone body, we analyze the shadowing caused by the drone body. Shadowing describes received signal fluctuations around the mean signal as the receiver changes its location, consequently experiencing different surrounding environments and objects in the signal's path [51]. Here, the cause of shadowing is completely different: it is exclusively due to the drone body. While many other works have investigated elevation-dependent shadowing in Unmanned Aerial Vehicle (UAV) channels [18], [32], [42], the emphasis was on the conventional shadowing caused by the surrounding environment. In addition, the effect of drone rotation on shadowing at various elevations is never addressed. For example, Akram *et. al* has proposed an elevation-dependent shadowing model as the UAV moves to higher altitudes away from buildings in urban environments [32]. Until now, little is known about how shadowing is affected solely by the drone body at various elevations and for different antenna orientations. Through the above explained LOS experiments, we evaluate the shadowing based on drone rotations.

The parameter that describes shadowing (i.e., ξ_s) is usually modeled in empirical path loss models as a zero-mean, Gaussian random variable with a standard deviation of σ_s (i.e., $\mathcal{N}(0, \sigma_s)$ [51]). The question is: if nothing else surrounding the drone is changing, does the drone body result in a different shadowing at slightly different elevation angles? We will find that the answer is yes. To analyze this drone-induced shadowing, the mean RSS per hovering location is subtracted from the instantaneous values for the two cases of facing and facing-away from the ground transmitter.

Effect of Drone Rotation with Vertical and Horizontal Antennas. First, we notice that, in general, significantly higher shadowing occurs when facing-away from the ground transmitter compared to when facing it. When facing the transmitter (i.e., $\phi = 0^\circ$) and across all elevation angles for all antenna setups, shadowing does not exceed 4 dB with a standard deviation never exceeding $\sigma_s = 2$ dB. On the other hand, when facing-away from the transmitter (i.e., $\phi = 180^\circ$), shadowing can reach up to 9 dB with a standard deviation of up to $\sigma_s = 6.36$ dB.

Second, we describe an interesting finding: when facing away from the ground transmitter, shadowing increases with elevation for all VV links. For VH links, however, this dependency is not observed. Fig. 10 shows the measured shadowing for the VV and VH links in the V-VH experiment. In Fig. 10(a) at 55° elevation, more shadowing (reaching up to 9.8 dB) is measured compared to 23°, at which shadowing does not exceed 2.5 dB. In Fig. 10(b), we find that the measured shadowing for the VH link does not change with elevation. The standard deviation of the measured shadowing parameter for facing-away vertical and horizontal Rx antennas is shown in Fig. 11. For the vertically-receiving antennas, Fig. 11(a), we find that σ_s increases with elevation for values in the range of 1 dB at $\theta = 3^\circ$ to approximately 6 dB at $\theta = 90^\circ$. This phenomena can be explained by how the antennas are placed on the side of the drone body: as the drone flies to relatively higher elevations and because it is facing away from the transmitter, more of the drone body obstructs the signal's path before it reaches the receiving antennas. However, since our horizontal antennas are mounted outwards of the body (see Fig. 3), the blockage they experience from the body is the same regardless of elevation. This can be seen in Fig. 11(b),

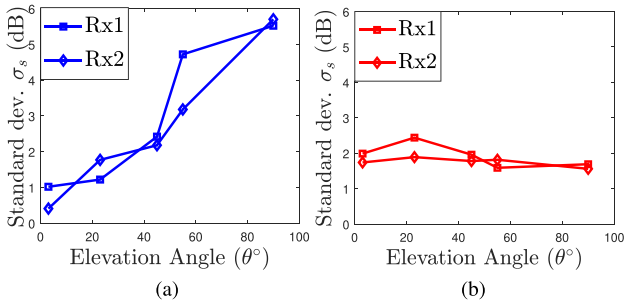

Fig. 11. Measured shadowing standard deviation (σ_s) at different elevations for the scenario of facing-away from the ground Tx. (a) σ_s for vertically mounted antennas. (b) σ_s for horizontally mounted antennas. Rx1 and Rx2 refer to antenna positions 1 and 2, respectively.

where the standard deviation barely changes with elevation. It might be worth mentioning that we have also seen this elevation dependency of shadowing in other LOS experiments at a carrier frequency of 900 MHz.

Effect of Diverse Antenna Positions for Same Orientation. Finally, for the same antenna orientation, different locations on the drone do not change the standard deviation of the shadowing parameter. For example, in the V-VV experiment, the average standard deviation of the V antenna in position 1 is $\overline{\sigma_s} = 1.38$ dB, while the V antenna in position 2 experiences a value of $\overline{\sigma_s} =$ 1.40 dB. The vertically-down (D) antenna experiences similar shadowing to the V antenna with an average standard deviation of $\overline{\sigma_s} =$ 1.46 dB. Here, average refers to the mean over all elevation angles.

E. Modeling the Impact of Drone Rotation

Through our anechoic chamber measurements, we have seen that the drone body and its rotation can result in considerable variations in the azimuth radiation pattern of the mounted antennas, introducing reductions in received power of up to 10 dB at some azimuth angles. This issue is worth investigating via in-field experiments, where we can also study the impact of elevation on this rotational loss. As explained in Section V-A, at each hovering location, the drone is rotated 180°, facing away from the ground transmitter, and the received I/Q samples are recorded for a period of 20 seconds. We analyze the effect of this rotation on the average RSS at every elevation angle and propose a model that captures this rotational loss. The conclusion reached is that this rotational loss is elevation-dependent for vertically-mounted antennas.

We define the average rotational loss per elevation angle per link as the difference in average RSS between the facing ($\phi = 0^\circ$) and facing-away ($\phi = 180^\circ$) measurements. The rotational loss, $\Gamma_\phi(\theta)$, can be calculated as $\overline{RSS}(\phi_0, \theta) - \overline{RSS}(\phi_{180}, \theta)$, where ϕ_0 indicates facing, and ϕ_{180} indicates the direction of facing-away from the Tx. We calculate this value for all VV experiments and find that it is elevation-dependent with higher elevations leading to higher $\Gamma_\phi(\theta)$ values. This result can be explained by the same intuition described in Section V-D, where more of the drone body starts to obstruct the receiving antennas at relatively higher elevations.

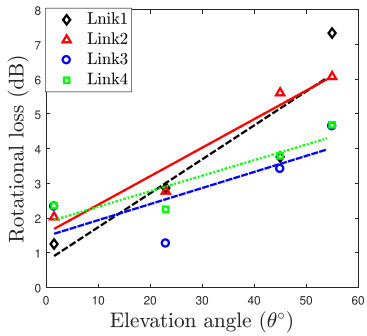

Fig. 12. Rotational loss and its linear fit representation $\Gamma_\phi(\theta)$.

TABLE III
FITTING PARAMETERS OF THE ROTATIONAL LOSS MODEL

Experiment	Link	Rx Ant.	μ	β	RMSE
V-VV	VV	1	0.0463	1.4768	0.814
V-VV	VV	2	0.0448	1.8769	0.4267
V-VH	VV	1	0.0822	1.5628	0.4195
V-HD	VD	2	0.0978	0.7583	0.9386

We plot this rotational loss for all VV links in Fig. 12 and see that this factor can increase from a range of 1 to 2.5 dB at $\theta = 3^\circ$ to the range of 5 to 7.5 dB at $\theta = 55^\circ$. A linear regression line that fits the average measured values as a function of elevation angle was created, and the results of this fitting for all VV links are shown in the same figure. In Fig. 12, links 1 to 4 represent the vertical links in the V-VV (twice), V-VH, and V-HD, experiments, respectively. It is not shown here, but, we additionally investigated another elevation angle where the drone is exactly above the ground transmitter (i.e., $\theta = 90^\circ$), and, intuitively, rotation seemed insignificant. In other words, no change in average RSS was observed. Moreover, no specific trend was observed for the VH links, as the rotational loss is approximately constant with a value around 2 dB across the investigated elevation angles.

For the VV links, the model that describes the elevation-dependent rotational loss Γ (in dB) as a function of the elevation angle, θ, can be described as:

$$\Gamma_\phi(\theta) = \mu\theta + \beta \tag{8}$$

Here, μ is the slope of the straight line, β is the intercept, and θ is the elevation angle between the ground Tx and the drone Rx. The values of these parameters for all vertical-to-vertical links are summarized in Table III.

We now quantify the benefit of including this rotational term in predicting the angle-dependent loss. The results of the measured and predicted values for L_{VV} of the VV link in the V-VH experiment are shown in Fig. 13. In this figure, we have 4 results: (i) L_{VV} is measured at $\phi = 0^\circ$, which is simply the average measured loss (difference between transmit power and average received power for 20 s) at the corresponding elevation angle when the Rx drone is facing the ground Tx. (ii) L_{VV} is measured at $\phi = 180^\circ$ with the drone facing-away from the Tx, which is clearly larger due to the drone body. (iii) A prediction is produced by using L_{VV} excluding $\Gamma_\phi(\theta)$), which is the result of predicting this angle-dependent loss using equation (5) but

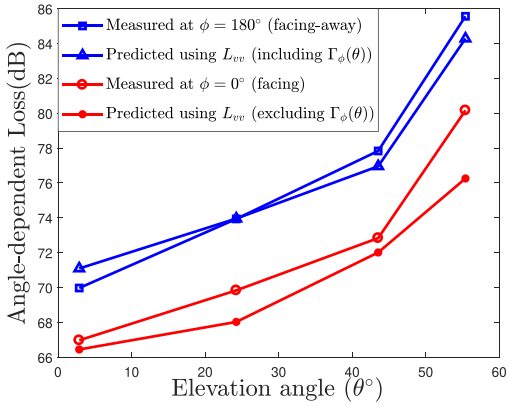

Fig. 13. Impact of using $\Gamma_\phi(\theta)$ on predicting the angle-dependent loss when a drone is rotated 180° at different elevation angles.

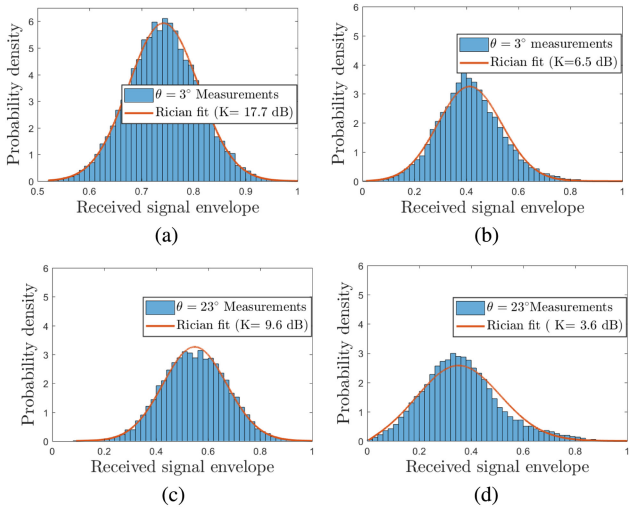

Fig. 14. Measured received signal envelope for VV and VH Ground-to-Drone links and its Rician fitting. (a) VV at $\theta = 3°$. (b) VH at $\theta = 3°$. (c) VV at $\theta = 23°$. (d) VH at $\theta = 23°$.

without the above-modeled rotational loss. In other words, it excludes the rotational loss (i.e., $\Gamma_\phi(\theta) = 0$ dB). (iv) Finally, we have the prediction using L_{VV} including the average value of the rotational loss, $\Gamma_\phi(\theta)$, which is predicted using the above model (equation (8)).

First, we can see that only using the elevation radiation pattern provides good prediction when facing the Tx. However, to predict the angle-dependent loss when facing-away from the Tx, a significant underestimation in the link budget of up to 11 dB can occur. An example of this error can be seen at an elevation angle of 55°, where we predict 75 dB of average link loss, but it is actually 86 dB. This error is due to the fact that this model, as in many other drone-related works [14], [15], [20], neglects drone rotation and antenna placement effects. Therefore, we recommend including this body-induced rotational factor when predicting drone-based links that involve drone rotation at different elevation angles.

Introducing the body-induced rotational factor into predicting angle-dependent losses would result in a more accurate capturing of the average (large-scale) behavior of drone-based links. For example, in the above discussed link, the average absolute error of our prediction is 0.89 dB. However, if we use a conventional model that excludes the rotational loss, the average error is 6.11 dB. As a result, our model is 85% more accurate because of the drone-body inclusion. The limitation of this model, however, is that it is only valid for the case of LOS ground-to-drone channels with no surrounding buildings, where the impact of the body is prominent. However, many applications can find this model useful including but not limited to smart agriculture systems, where ground nodes send data to a collector drone that hovers in a certain direction. In such a scenario, the transmit power can be carefully designed to compensate for the above Γ_ϕ effects.

VI. Small-Scale Fading for Drone-Mounted Antennas in 3D Space

In this section, we study how the orientation of multiple drone-mounted antennas can affect small-scale fading severity. The effects are measured in terms of the Rician K-factor and are investigated for polarization-matched and cross-polarized GtD links. Furthermore, to focus on the role of the mounted antennas and not confuse it with that of ground-induced fluctuations, we quantify the impact of ground reflection on the Rician K-factor via another set of DtD experiments at high altitude, where the effect of ground reflections are minimal. We then compare the Rician K-factor values to those obtained in the GtD experiments. Lastly, to determine the impact of our antenna placement decisions on possible diversity gains, we analyze the correlation coefficient at all elevation angles for both heading direction scenarios (facing and facing-away) and make recommendations that could lead to the efficient design of drone-based networks.

A. K-Factor in 3D Ground-to-Drone Channels

We analyze the instantaneous received signal envelope recorded at both RF chains for three GtD experiments. We include a unique elevation angle, where the receiving drone hovers above the ground transmitter at an angle of 90° with a vertical distance of 10 m. This angle was examined to demonstrate the impact of extreme elevation as opposed to the $\theta = 3°$ angle. An example of how the measured LOS channel follows a Rician distribution is shown in Fig. 14, where a histogram of 3000 samples (a time period of 93.7 ms) of the instantaneous received signal is plotted. Then, a Rician distribution is fitted to the measurements using the maximum-likelihood estimate (MLE) [52]. In this figure, we can see that higher K values (17.7 and 9.6 dB) are obtained for VV links compared to the VH links (6.5 and 3.6 dB) at 3° and 23° elevations, respectively. It is worth mentioning that the KolmogorovSmirnov test was performed to compare our measurements to the fitted Rician distribution. The results of this comparison indicated that we accept the null hypothesis that the two sample vectors (measurements and fitted distribution samples) come from the same distribution. This is true for the investigated elevation angles of 3°, 23°, 45°, and 55°.

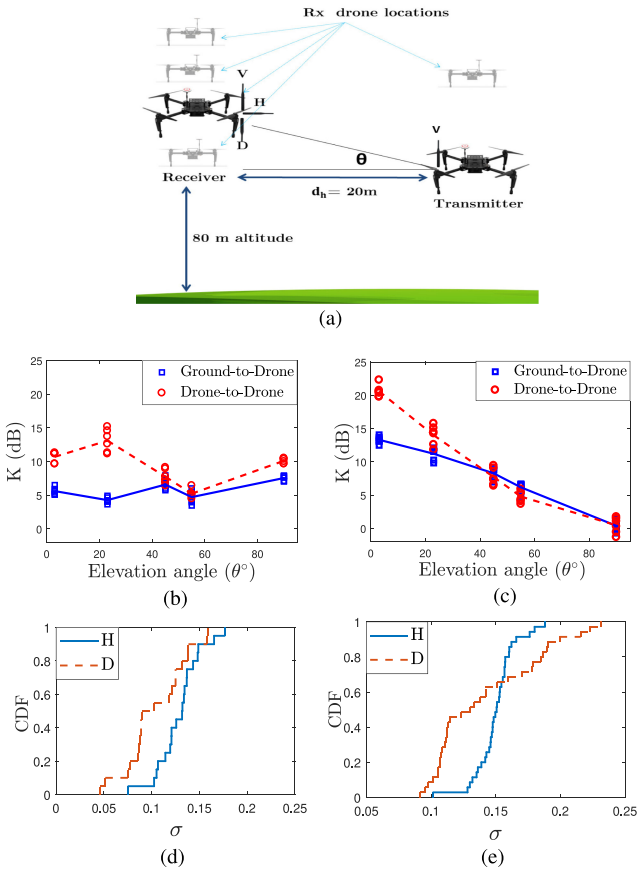

Fig. 15. Flight path for the DtD experiments. Faded figures indicate hovering locations. (b) The K-values for the VH link. (c) The K values for the VV link. The empirical CDF of σ for the V-HD experiment in the GtD and DtD scenarios is shown in (d) and (e), respectively.

In general, our results indicate that the K-factor is strongly dependent on the elevation angle for polarization-matched VV links since it can change by as much as 15 dB, whereas it is approximately flat for the VH link across all elevation angles. For example, refer the GtD results in Fig. 15(c), where each point (indicated by blue squares) represents the average of six values of the K-factor of the VV link. We see that the strongest K values are recorded at 3° with a range of 13-15 dB. However, after this angle, as the drones moves to higher altitudes, the K-factor starts to decrease, reaching approximately 4 to 5 dB at $\theta = 55^\circ$. This reduction can be explained by the analytical models developed above, where the radiation pattern product becomes weaker as the receiving drone moves to higher elevations. At 90° elevation (i.e., the Rx drone hovers above the ground Tx), the K factor becomes almost 0 dB, indicating an extremely weak LOS component.

For the VH link (Fig. 15(b)), this strong elevation dependency is not observed. The K-factor is nearly constant because of the low variation in the radiation pattern product over a wide range of elevation angles (shown in Fig. 9). However, since our GtD experiments are conducted close to the ground, the impact of fluctuations caused by the ground needs to be understood so that we can isolate the impact of drone-mounted antenna position/orientation on small-scale fading. To quantify these ground effects, we analyze another set of results from DtD experiments that we carried out in the same geographical location but at altitudes where no surrounding objects exist, and the ground is at least 80 m below the drone (i.e., the effect of ground reflections is weak).

TABLE IV
RICIAN K-FACTOR FOR VV AND VH LINKS IN GTD AND DTD EXPERIMENTS

Ground-to-Drone K (dB)					
Link	$\theta = 3^\circ$	$\theta = 23^\circ$	$\theta = 45^\circ$	$\theta = 55^\circ$	$\theta = 90^\circ$
VV	13.31	11.21	8.27	6.16	0.37
VH	5.61	4.27	6.58	4.71	7.55
Drone-to-Drone K (dB)					
Link	$\theta = 3^\circ$	$\theta = 23^\circ$	$\theta = 45^\circ$	$\theta = 55^\circ$	$\theta = 90^\circ$
VV	20.60	14.03	7.75	4.78	0.45
VH	10.69	13.09	7.75	5.22	10.10

B. Ground-to-Drone vs. Drone-to-Drone K-Factor

To investigate the impact of the ground on the Rician K-factor, we conduct a set of DtD experiments that matches the GtD experiments. We then calculate the K-factor at the same elevation angles. The experiments are conducted at 80 to 110 m altitude, where the environment is free of reflecting objects, and the two drones are facing each other. The DtD experiment is shown in Fig. 15(a). The Tx drone is fixed at its hovering location at 80-m altitude, where the Rx drone is automated to fly at locations that would result in approximately the same elevation angles as in the GtD experiments. Similar to Section VI-A, we conduct three experiments: V-VV, V-VH, and V-HD.

We calculate the K-factor and report this finding. At 3° and 23° elevation angles, the K values from the DtD experiments are always stronger than those obtained from the GtD experiments. For example, in Fig. 15(c), we see at 3° to 23° elevation, the DtD K-factor can reach values of up to 24 dB, which is 10 dB higher than that of the GtD experiments. As the elevation angle increases, however, this difference starts to diminish, indicating a lesser role of the ground than that of the actual hovering drone and its mounted antennas. To further understand the impact of the ground on the K-factor, consider Fig. 15(d)-15(e) as an example. Here, the CDF of measured σ, the parameter that describes the reflected components in equation (7), is plotted. We can see that it is definitely higher in the GtD experiments than in the DtD experiments. For example, 40% of measured values are greater than 0.15 in the GtD experiment, as opposed to 20% in the DtD experiment. If we assume a fixed-LOS component, a higher σ results in a lower K, as is happening at altitudes close to the ground. The measured K-factor values for VV and VH links in the GtD and DtD experiments are summarized in Table IV.

To realize the impact of these K variations on system performance, we simulate a 64-QAM Rician fading channel with different K values. The results are shown in Fig. 16. We can see that a reduction of K from 20 dB to 3 dB (from around 3° to 90° drone elevation for VV links) can, at an SNR of 18 dB, increase the bit error rate (BER) by three orders of magnitude. If we switch to using the horizontal antenna at 90°, the estimated K is around 12 dB, which leads to only one order of magnitude increase in BER.

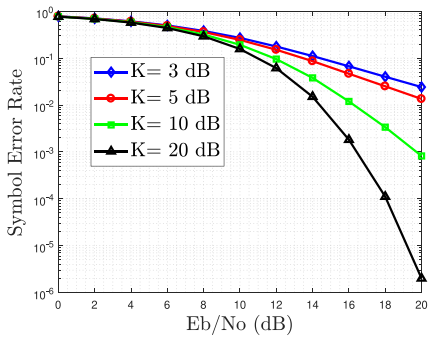

Fig. 16. The impact of K-factor variations on symbol error rate for a 64-QAM system in a Rician fading channel.

TABLE V
CORRELATION COEFFICIENT VS. ELEVATION ANGLE

Facing Tx ($\phi = 0°$)			
θ	$\rho_{v,h}$	$\rho_{v,v}$	$\rho_{h,d}$
3°	0.45	0.43	0.63
23°	0.32	0.35	0.25
45°	0.3	0.21	0.19
55°	-0.22	0.1	-0.15
90°	-0.08	0.1	-0.3
Facing-way from Tx ($\phi = 180°$)			
θ	$\rho_{v,h}$	$\rho_{v,v}$	$\rho_{h,d}$
3°	0.34	0.33	0.43
23°	0.08	0.19	0.16
45°	0.5	0.06	0.45
55°	0.14	0.02	0.1
90°	0.22	0.14	0.06

It is worth mentioning that while previous works have analyzed the Rician K-factor variations with drone height [12], [18], the nature of the environment in those experiments makes it difficult to isolate radiation pattern and antenna orientation effects from the impact of the actual obstructions and reflectors in the signal's path. In this study, these K variations are solely due to the antenna location/orientation and drone proximity to the ground, not induced by the surrounding environment (e.g., buildings, trees, and cars).

C. Correlation and Diversity Gains in 3D GtD Channels

As future drones might be expected to carry large number of antennas for a variety of applications, a thorough analysis of the impact of antenna orientation, spacing, and 3D placement on correlation and diversity gains is critical. Here, we use the envelope correlation coefficient rather than the complex-signal correlation coefficient, which has both the in-phase and quadrature components in its calculation. While this metric ignores the phase of signal correlation, it is faster and simpler to calculate. The metric is acceptable in literature to approximate the complex signal correlation by the envelope correlation for small antenna separation [53]. This envelope correlation coefficient is calculated as:

$$\rho_{x1,x2} = \frac{\sum_{n=1}^{N}(r_{x1} - \overline{r_{x1}})(r_{x2} - \overline{r_{x2}})}{\sqrt{\sum_{n=1}^{N}(r_{x1} - \overline{r_{x1}})^2}\sqrt{\sum_{n=1}^{N}(r_{x2} - \overline{r_{x2}})^2}} \quad (9)$$

Here, N is the total number of samples, and $\overline{r_{x1}}$ is the mean value of the fast-fading signal envelope r_{x1}, which corresponds to the first antenna orientation. The term r_{x2} corresponds to the second receiver's antenna orientation. For example, $\rho_{h,d}$ is the correlation coefficient between the signal envelopes of the H and D antennas in the V-HD experiment. The correlation coefficient for all elevation angles and the two heading directions are summarized in Table V. These values are obtained for the entire hovering period of 20 s per heading direction (i.e., N = 32 kS/s $\times$ 20 s = 640K samples).

First, we notice that the envelope correlation coefficient between the two receiving antennas in the facing Tx scenario is highest at 3° elevation, even for the cross-polarized setup. Then, correlation decreases as the elevation angle increases. At 55° and 90°, correlation becomes slightly negative for the cross-polarized setups, indicating the increase of the received signal envelope (horizontal), while the other (vertical) decreases. When the drone is facing away from the transmitter, $\phi = 180°$, no specific trend is observed. Interestingly, even though our experiments are in perfect LOS, we report that for all antenna setups, at all elevation angles and for both azimuth directions, the correlation coefficient never exceeds 0.7. As a result, diversity gains can be achieved in the 9.5 to 11.5 dB range using Maximal Ratio Combiner (MRC) or Selection Combining (SC) in Rayleigh and Rician fading channels at an outage probability of 0.01. This is an important result due to the fact that diversity gains for a fixed outage probability would fall more rapidly at correlation values higher than 0.7 [54], [55]. With this result and our previous conclusion [21], we can conclude that in LOS Ground-to-Drone and Drone-to-Drone channels, an antenna spacing of 0.67λ (8 cm in this case) is a good design choice if diversity gains are of interest, regardless of antenna orientation.

VII. CONCLUSION

In this paper, we have shown that, due to drone-antenna interaction, the constant azimuth radiation pattern assumption made in all drone-related works is no longer true. Variations of up to 10.25 dB can be measured when antennas are mounted on a drone. Furthermore, we show that the body of the drone not only affects the co-polar component of the received signal but also the cross-polar component, increasing polarization mixing and consequently reducing XPD by up to 15 dB. Then, through in-field experiments, we measure and model the losses induced by the drone body and find that, for the case of a drone facing-away a ground transmitter, our model that includes rotational loss, can be 85% more accurate than conventional models that neglect the drone body. The impact of antenna placement on the Rician K-factor at different drone hovering angles is then analyzed and, for polarization matched vertical links, variations of up to 15 dB in the K-factor were measured as the elevation angle changes from 3° to 90°. However, cross-polarized links result in approximately a flat behavior with variations of less than 4.5 dB across all angles. The ground is found to reduce the K-factor by up to 10 dB at low elevations. However, at higher elevations, GtD and DtD links have similar K-factor values. Finally, through analyzing the measured correlation coefficient, we find that an antenna spacing of 0.67λ would result in a correlation coefficient less than 0.7, regardless of antenna orientation.

REFERENCES

[1] "The drone market insights from customers and providers," CompTIA, Jun. 2019. [Online]. Available: https://www.comptia.org/content/research/the-drone-market-insights-from-customers-and-providers

[2] I. Mademlis, N. Nikolaidis, A. Tefas, I. Pitas, T. Wagner, and A. Messina, "Autonomous UAV cinematography: A tutorial and a formalized shot-type taxonomy," in *ACM Comput. Surv.*, vol. 52, no. 5, Sep. 2019, Art. no. 105.

[3] C. Koparan, A. B. Koc, C. V. Privette and C. B. Sawyer, "Adaptive water sampling device for aerial robots," *Drones*, vol. 4, no. 1, 2020.

[4] "Canadian drone test uses LTE network to deliver defibrillators," Ericsson [Online]. Available: https://www.ericsson.com/en/news/2019/10/defibrilators-delivered-via-lte-enabled-drones-in-canada.

[5] Y. Zeng, R. Zhang, and T. J. Lim, "Wireless communications with unmanned aerial vehicles: Opportunities and challenges," *IEEE Commun. Mag.*, vol. 54, no. 5, pp. 36–42, May 2016.

[6] M. Mozaffari, W. Saad, M. Bennis, and M. Debbah, "Mobile Internet of Things: Can UAVs provide an energy-efficient mobile architecture?," in *Proc. IEEE Global Commun. Conf.*, 2016, pp. 1–6.

[7] L. Zeng, X. Cheng, C.-X. Wang, and X. Yin, "A 3D geometry-based stochastic channel model for UAV-MIMO channels," in *Proc. IEEE Wireless Commun. Netw. Conf.*, 2017, pp. 1–5.

[8] H. Jiang, Z. Zhang, L. Wu, and J. Dang, "Three-dimensional geometry based UAV-MIMO channel modeling for A2G communication environments," *IEEE Commun. Lett*, vol. 22, no. 7, pp. 1438–1441, Jul. 2018.

[9] J. Chen, B. Daneshrad, and W. Zhu, "MIMO performance evaluation for airborne wireless communication systems," in *Proc. IEEE Mil. Commun. Conf.*, 2011, pp. 1827–1832.

[10] T. Willink, C. Squires, G. Colman, and M. Muccio, "Measurement and characterization of low altitude air-to-ground MIMO channels," *IEEE Trans. Veh. Technol.*, vol. 65, no. 4, pp. 2637-2648, Apr. 2016.

[11] Y. Shi, R. Enami, J. Wensowitch, and J. Camp, "UABeam: UAV-based beamforming system analysis with in-field air-to-ground channels," in *Proc. IEEE Sens., Commun., Netw.*, 2018, pp. 1–9.

[12] Z. Qiu, X. Chu, C. Calvo-Ramirez, C. Briso, and X. Yin, "Low altitude UAV air-to-ground channel measurement and modeling in semiurban environments," *Wireless Commun. Transp. Syst.*, vol. 2017, Nov. 2017, doi: 10.1155/2017/1587412.

[13] E. Yanmaz, R. Kuschnig, and C. Bettstetter, "Achieving air-ground communications in 802.11 networks with three-dimensional aerial mobility," in *Proc. IEEE INFOCOM (Mini Conf.)*, 2013, pp. 120–124.

[14] W. Khawaja, O. Ozdemir, F. Erden, I. Guvenc, and D. Matolak, "UWB air-to-ground propagation channel measurements and modeling using UAVs," in *Proc. IEEE Aerosp. Conf.*, 2019, pp. 1–10.

[15] J. Chen, D. Raye, W. Khawaja, P. Sinha, and I. Guvenc, "Impact of 3D UWB antenna radiation pattern on air-to-ground drone connectivity," in *Proc. IEEE Veh. Technol. Conf.*, 2018, pp. 1–5.

[16] H. T. Kung, C. K. Lin, T. H. Lin, S. J. Tarsa and D. Vlah, "Measuring diversity on a low-altitude UAV in a groundtoair wireless 802.11 mesh network," in *Proc. IEEE Global Commun. Conf.*, 2010, pp. 1799–1804.

[17] C.-M. Cheng, P.-H. Hsiao, H. Kung, and D. Vlah, "Performance measurement of 802.11a wireless links from UAV to ground nodes with various antenna orientations," in *Proc. IEEE Int. Conf. Comput. Commun. Netw.*, 2006, pp. 303–308.

[18] N. Goddemeier and C. Wietfeld, "Investigation of air-to-air channel characteristics and a UAV specific extension to the rice model," in *Proc. IEEE Global Commun. Conf. (Workshops)*, 2015, pp. 1–5.

[19] Z. Cui, C. Briso-Rodriguez, K. Guan, and Z. Zhong, "Ultra-wideband air-to-ground channel measurements and modeling in hilly environment," in *Proc. IEEE Int. Conf. Commun.*, 2020, pp. 1–6.

[20] P. Sinha, Y. Yapici, and I. Guvenc, "Impact of 3D antenna radiation patterns on TDOA-based wireless localization of UAVs," in *Proc. IEEE INFOCOM (Workshops)*, 2019, pp. 614–619.

[21] M. Badi, J. Wensowitch, D. Rajan, and J. Camp, "Experimental evaluation of antenna polarization and elevation effects on drone communications," in *Proc. 22st Int. ACM Conf. Model., Anal. Simul. wireless Mobile Syst.*, 2019, pp. 211–220.

[22] M. Mozaffari, W. Saad, M. Bennis, Y.-H. Nam, and M. Debbah, "A tutorial on UAVs for wireless networks: Applications, challenges, and open problems," *IEEE Commun. Surv. Tut.*, vol. 21, no. 3, pp. 2334–2360, Jul.-Sep. 2019

[23] P. A. Catherwood, B. Black, E. Bedeer, A. A. Cheema, J. Rafferty, J. A. D. McLaughlin, "Radio channel characterization of mid-band 5G service delivery for ultra-low altitude aerial base stations," *IEEE Access*, vol. 7, pp. 8283–8299, 2019.

[24] M. Shafi *et al.*, "Polarized MIMO channels in 3-D: Models, measurements and mutual information," *IEEE J. Sel. Areas Commun.*, vol. 24, no. 3, pp. 514–527, Mar. 2006.

[25] W. Khawaja, O. Ozdemir, and I. Guvenc, "UAV air-to-ground channel characterization for mmWave systems," in *Proc. IEEE Veh. Technol. Conf. VTC-Fall (Workshops)*, 2017, pp. 1–5.

[26] "Spatial channel model for multiple input multiple output MIMO simulations," 3GPP, vol. TR 25.996, v6.1.0, Sep. 2003.

[27] J. Wang, J. Zhao, and X. Gao, "Modeling and analysis of polarized MIMO channels in 3D propagation environment," in *Proc. IEEE Int. Symp. Personal Indoor Mobile Radio Commun.*, 2010, pp. 319–323.

[28] X. Su, D. Choi, X. Liu, and B Peng, "Channel model for polarized MIMO systems with power radiation pattern concern," *IEEE Access*, vol. 4, pp. 1061–1072, Mar. 2016

[29] S. Baidya, Z. Shaikh, and M. Levorato, "FlyNetSim: An open source synchronized UAV network simulator based on ns-3 and ardupilot," in *Proc. 21st ACM Int. Conf. Model. Anal. Simul. wireless Mobile Syst.*, 2018, pp. 37–45.

[30] E. Yanmaz, R. Kuschnig, and C. Bettstetter, "Channel measurements over 802.11a-based UAV-to-ground links," in *Proc. IEEE Global Commun. Conf. (Workshops)*, 2011, pp. 1280–1284.

[31] E. Yanmaz, S. Hayat, J. Scherer, and C. Bettstetter, "Experimental performance analysis of two-hop aerial 802.11 networks," in *Proc. IEEE Wireless Commun. Netw. Conf.*, 2014, pp. 3118–3123.

[32] A. Al-Hourani and K. Gomez, "Modeling cellular-to-UAV path-loss for suburban environments," *IEEE Wireless Commun. Lett.*, vol. 7, no. 1, pp. 82–85, Feb. 2018.

[33] S. C. Kwon and G. L. St Uber, "Geometrical theory of channel depolarization," *IEEE Trans. Veh. Technol.*, vol. 60, no. 8, pp. 3542-3556, Oct. 2011.

[34] M.-T. Dao, V.-A. Nguyen, Y.-T. Im, S.-O. Park, and G. Yoon, "3D polarized channel modeling and performance comparison of MIMO antenna configurations with different polarizations," *IEEE Trans. Antennas Propag.*, vol. 59, no. 7, pp. 2672-2682, Jul. 2011.

[35] Y. Xing, O. Kanhere, S. Ju, T. S. Rappaport, and G. R. MacCartneyJr, "Verification and calibration of antenna cross-polarization discrimination and penetration loss for millimeter wave communications," in *Proc. IEEE Veh. Technol. Conf. VTC-Fall*, 2018, pp. 1–6.

[36] Y.-G. Lim, Y. J. Cho, T. Oh, Y. Lee, and C.-B. Chae, "Relationship between cross-polarization discrimination (XPD) and spatial correlation in indoor small-cell MIMO systems," *IEEE Wireless Commun. Lett.*, vol. 7, no. 4, pp. 654–657, Aug. 2018

[37] Y. Yao, J. Zheng, and Z. Feng, "Diversity measurements for on-body channels using a tri-polarization antenna at 2.45 GHz," *IEEE Antennas Wireless Propag. Lett.*, vol. 11, pp. 1285-1288, 2012.

[38] T. Neubauer and P. C. F. Eggers, "Simultaneous characterization of polarization matrix components in pico cells," in *Proc. IEEE Veh. Technol. Conf. VTC-Fall*, 1999, pp. 1361–1365.

[39] K. Morioka *et al.*, "5GHz ground-to-air communication link by AeroMACS in high-speed movement scenarios," in *Proc. Asia-Pacific Conf. Commun.*, 2017, pp. 1–6.

[40] P. Laly *et al.*, "Polarimetric ground-to-ground and ground-to-air channel characterization in forest environment," in *Proc. Eur. Conf. Antennas Propag.*, 2017, pp. 2431–2434.

[41] Y. Shi, R. Enami, J. Wensowitch, and J. Camp, "Measurement-based characterization of LOS and NLOS drone-to-ground channels," in *Proc. IEEE Wireless Commun. Netw. Conf.*, 2018, pp. 1–6.

[42] J. Holis and P. Pechac, "Elevation dependent shadowing model for mobile communications via high altitude platforms in built-up areas," *IEEE Trans. Antennas Propag.*, vol. 56, no. 4, pp. 1078–1084, Apr. 2008.

[43] R. Sun, D. W. Matolak, and W. Rayess, "Air-ground channel characterization for unmanned aircraft systems Part IV: Airframe shadowing," *IEEE Trans. Veh. Technol.*, vol. 66, no. 9, pp. 7643–7652, Sep. 2017

[44] Z. Cui, C. Briso-Rodriguez, K. Guan, C. Calvo-Ramrez, B. Ai, and Z. Zhong, "Measurement-based modeling and analysis of UAV air-ground channels at 1 and 4 GHz," *IEEE Antennas Wireless Propag. Lett.*, vol. 18, no. 9, pp. 1804–1808, Sep. 2019.

[45] F. Jiang and A. L. Swindlehurst, "Optimization of UAV heading for the ground-to-air uplink," *IEEE J. Sel. Areas Commun.*, vol. 30, no. 5, pp. 993–1005, Jun. 2012.

[46] M. Mozaffari, W. Saad, M. Bennis, and M. Debbah, "Unmanned aerial vehicle with underlaid device-to-device communications: Performance and tradeoffs," *IEEE Trans. Wireless Commun.*, vol. 15, no. 6, pp. 3949–3963, Jun. 2016.

[47] M. Alzenad, A. El-Keyi, F. Lagum, and H. Yanikomeroglu, "3-D placement of an unmanned aerial vehicle base station (UAV-BS) for energy efficient maximal coverage," *IEEE Wireless Commun. Lett.*, vol. 6, no. 4, pp. 434–437, Aug. 2017.
[48] R. I. Bor-Yaliniz, A. El-Keyi, and H. Yanikomeroglu, "Efficient 3-D placement of an aerial base station in next generation cellular networks," in *Proc. IEEE Int. Conf. Commun.*, 2016, pp. 1–5.
[49] M. D. Nguyen, T. M. Ho, L. B. Le, and A. Girard, "UAV trajectory and sub-channel assignment for UAV based wireless networks," in *Proc. IEEE Wireless Commun. Netw. Conf.*, 2020, pp. 1–6.
[50] Q. Wu, J. Xu, and R. Zhang, "Capacity characterization of UAV-enabled two-user broadcast channel," *IEEE J. Sel. Areas Commun.*, vol. 36, no. 9, pp. 1955-1971, Sep. 2018.
[51] A. Goldsmith, Wireless communications. Cambridge, U.K.: Cambridge Univ. Press, 2005.
[52] K. E. Baddour and T. J. Willink, "Improved estimation of the Ricean-factor from I/Q fading channel samples," *IEEE Trans. Wireless Commun.*, vol. 7, no. 12, pp. 5051–5057, Dec. 2008.
[53] H. T. Hui, "Fast calculation of diversity gain in correlated Rician-fading channels," *IEEE Antennas Wireless Propag. Lett.*, vol. 5, no. 1, pp. 123–126, Apr. 2006.
[54] H. T. Hui, "The performance of the maximum ratio combining method in correlated Rician-fading channels for antenna-diversity signal combining," *IEEE Trans. Antennas Propag.*, vol. 53, no. 3, pp. 958-964, Mar. 2005.
[55] P. Mattheijssen, M. Herben, G. Dolmans, and L. Leyten, "Antenna-pattern diversity versus space diversity for use at handhelds," *IEEE Trans. Veh. Technol*, vol. 53, no. 4, pp. 1035–1042, Jul. 2004.
[56] C. Balanis, Antenna theory, analysis, and design, 2nd ed. New York, NY, USA:Wiley, 1997.
[57] S. Benik and P. Hajach, "Radiation of antenna arrays with generally oriented dipoles," *J. Elect. Eng.*, vol. 53, no. 7-8, pp. 202-207, 2002.
[58] VERT2450 Antenna Data-sheet, Ettus Research LLC [Online]. Available: https://smu.box.com/s/75ccfjiwmqswcd7itkwu0n5ph7jzu3ay.
[59] D. Munalli, G. Dimitrakis, D. Chronopoulos, S. Greedy, and A. Long, "Electromagnetic shielding effectiveness of carbon fibre reinforced composites," *Composites Part B.: Eng.*, vol. 173, p. 106906, Sep. 2019.

Mahmoud Badi received the M.S. degree in telecommunications from Southern Methodist University (SMU), Dallas, Texas, USA, on Fulbright scholarship in 2017, and the B.S. degree in electrical and electronics engineering from the University of Tripoli, Libya, in 2012. He is currently working toward the Ph.D. degree in electrical and computer engineering, SMU. His current research areas are UAV communications and centralized and distributed multiple antenna systems.

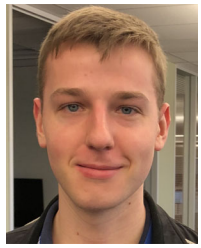

John Wensowitch received the B.S. degree in electrical engineering and the M.S. degree in electrical and computer engineering from Southern Methodist University (SMU), Dallas, Texas, USA, in 2019 and 2020, respectively. He is currently working toward the Ph.D. degree in electrical and computer engineering with SMU. His current research interests include software defined radio and embedded systems programming, drone-based communications and the deployment, and analysis of large-scale wireless networks.

Dinesh Rajan (Senior Member, IEEE) received the B.Tech. degree in electrical engineering from the Indian Institute of Technology, Madras. He received the M.S. and Ph.D. degrees in electrical and computer engineering from Rice University, Houston, Texas. He is currently Department Chair and Cecil and Ida Green Professor with the Electrical and Computer Engineering Department, Southern Methodist University. He joined the Electrical Engineering Department with Southern Methodist University, Dallas, Texas, in August 2002, as an Assistant Professor. His current research interests include communications theory, wireless networks, information theory and computational imaging. He was recipient of the NSF CAREER award for his work on applying information theory to the design of mobile wireless networks. He is also a recipient of the Golden Mustang Outstanding Faculty Award and the Senior Ford Research Fellowship from SMU.

Joseph Camp (Member, IEEE) received the B.S. (hons.) degree in electrical and computer engineering from the UT-Austin, Austin, TX, USA, and the M.S. and Ph.D. degrees in electrical and computer engineering from Rice University, Houston, TX, USA. He is currently an Associate Professor of electrical and computer engineering with Southern Methodist University, Dallas, TX, USA. He joined the SMU Faculty in 2009. His research team has performed more than 200 million in-field wireless measurements around the world via Android deployment and local characterization via drones, campus buses, vehicles, and buildings. His research interests, wireless communications and networking, crowdsourcing, and drones, specifically focused on the deployment, measurement, and analysis of large-scale systems and development of embedded protocols. He was the recipient of the National Science Foundation CAREER Award in 2012 and the Golden Mustang Teaching Award in 2014.